

## Organic carbon burial in a middle Eocene East Asian paleolake: Response to global and regional climate changes

Qiqi Li <sup>a,b</sup>, Shang Xu <sup>c,\*</sup>, Fang Hao <sup>c</sup>

<sup>a</sup> Key Laboratory of Coalbed Methane Resources and Reservoir Formation Process, Ministry of Education, China University of Mining and Technology, Xuzhou 221008, China

<sup>b</sup> School of Resources and Geosciences, China University of Mining and Technology, Xuzhou 221116, China

<sup>c</sup> State Key Laboratory of Deep Oil and Gas, China University of Petroleum (East China), Qingdao 266580, China



### ARTICLE INFO

Editor: Bing Shen

#### Keywords:

Organic carbon burial  
Carbon cycle  
Climate change  
Paleolake  
Eocene

### ABSTRACT

Organic carbon burial in lakes represents an important natural mechanism for long-term organic carbon sequestration and a critical component of the global carbon cycle. However, the dynamics of lacustrine organic carbon burial are more complex than marine systems, and the mechanisms linking it to global and regional tectonic-climatic factors remain poorly understood. Here, we present an organic carbon burial record from the Dongying paleolake in the Bohai Bay Basin during the middle Eocene, integrated with high-resolution reconstructions of terrestrial paleoclimate and paleolake environments, to elucidate the controls on organic carbon burial in large lacustrine systems. Our findings indicate that middle Eocene terrestrial paleoclimate evolution in the Bohai Bay Basin was modulated by both global and regional forcing, resulting in two climate transitions at ~43 Ma and ~42 Ma. The first transition is attributed to the southward migration of subtropical high pressure caused by global cooling, while the second transition is associated with regional factors, including the Tibetan Plateau uplift and Paratethys Sea retreat. Terrestrial paleoclimate profoundly influenced the co-evolution of paleolake environments and organisms, causing significant differences in the source, accumulation, and preservation of organic matter during different phases, along with notable variations in organic carbon burial. We propose that organic carbon burial in the large paleolakes of the Bohai Bay Basin was a response to global and regional climate changes. These findings highlight the climatic sensitivity of lacustrine organic carbon burial, which may in turn play a key role in climate regulation. This study enhances our understanding of lacustrine carbon burial potential, patterns, and mechanisms, as well as the role of lakes in the global carbon cycle.

### 1. Introduction

Amidst the backdrop of ongoing global climate change and corresponding carbon emissions, the dynamics and mechanisms of the carbon cycle have garnered significant interest among scholars globally. Lakes serve as recipients, regulators, reactors, and storage in the global carbon cycle (Tranvik et al., 2009). Although the total area of global lakes is less than 2% of the Earth's surface, the organic carbon buried in these lakes each year can reach 50% of the annual organic carbon sink of the oceans (which cover approximately 71% of the Earth's surface), attributable to the high organic carbon deposition rates and preservation efficiency of lakes (Sobek et al., 2009; Mendonça et al., 2017). It is evident that lakes are significant reservoirs of organic carbon on the Earth's surface and may play a crucial role in global carbon sequestration (Sobek et al.,

2009). Moreover, only the burial of organic carbon in sediments removes carbon from the short-term biosphere-atmosphere carbon cycle (Mendonça et al., 2017). Therefore, although photosynthesis produces oxygen, it is the burial of organic carbon in sediments that allows this oxygen to accumulate in Earth's atmosphere (Cartapanis et al., 2016). Research has shown that lakes are capable of responding to changes in the global carbon cycle and potentially affect climate through the burial of substantial quantities of organic carbon (Xu et al., 2017). However, due to the limited temporal scope of modern lake observations, the response mechanisms of long-term lacustrine organic carbon burial to climate change remain unclear. Therefore, research on paleolakes can provide critical insights into lacustrine carbon cycling. Moreover, substantial burial of organic carbon can lead to the formation of lacustrine organic-rich mudstone and shale, which may serve as potential

\* Corresponding authors at: School of Geosciences, China University of Petroleum, Changjiangxi Road No.66, Qingdao 266580, China.

E-mail addresses: liqiqi6@163.com (Q. Li), xushang0222@163.com (S. Xu), haofang@cug.edu.cn (F. Hao).

hydrocarbon source rocks (Hao et al., 2011). For these reasons, the study of lacustrine organic carbon burial is of dual environmental and economic significance and has consequently attracted considerable interest from scholars.

Throughout geological history, marine organic carbon burial has been closely linked to global climate change (Cartapanis et al., 2016). This is exemplified by substantial organic carbon deposition in continental margin sedimentary basins during greenhouse periods associated with Oceanic Anoxic Events (OAEs) (Kemp et al., 2022). In contrast, the dynamics of organic carbon burial in lacustrine environments are more complex due to the interplay of global and regional factors and the unique characteristics of lakes. Many controlling factors of lacustrine organic carbon burial remain poorly understood, particularly the relationships between the long-term lacustrine organic carbon burial and climate change. East Asia during the middle-late Eocene provides an ideal case for investigating these relationships, as this period was characterized by frequent global paleoclimate changes and a significant reorganization of paleoclimatic patterns in East Asia (Licht et al., 2014; Westerhold et al., 2020). Furthermore, lakes are sensitive to changes in paleoclimate, and given that their sedimentation rates are typically much higher than those observed in marine settings, they can also provide high-resolution archives of paleoenvironmental conditions. The widely developed organic-rich shales in eastern China perfectly document these climate changes and are considered one of the most important lacustrine source rocks for oil and gas exploration (Ma et al., 2019; Shi et al., 2019). As a result, those shales have been the focus of considerable research, both for their significance in understanding Eocene greenhouse climate change and for their potential as hydrocarbon source rocks.

In the present study, the Dongying Depression in the Bohai Bay Basin serves as a representative case to investigate the response mechanisms of lacustrine organic carbon burial to global and regional climate changes. Previous studies have demonstrated the influence of climatic conditions on organic carbon burial in this basin. For instance, Ma et al. (2016) elucidated the control of lake hydrologic conditions and depositional processes on organic carbon burial under arid and humid climatic conditions. Wei et al. (2021) suggested that climate change regulates denitrification intensity by controlling lake salinity, thereby influencing the efficiency of organic carbon burial. Moreover, the impact of astronomically forced paleoclimate fluctuations on organic carbon burial has attracted significant attention. For example, Zhang et al. (2022) found that enhanced summer insolation and monsoonal precipitation during precession minima could significantly increase organic carbon burial. However, due to the complexity of Eocene paleoclimatic changes in East Asia, the response mechanisms of lacustrine organic carbon burial to global and regional climate changes over long timescales remain poorly understood.

This study utilizes the Eocene lacustrine fine-grained sedimentary sequence from the Dongying Depression in the Bohai Bay Basin to reconstruct high-resolution records of organic carbon burial, terrestrial paleoclimate, and paleolake environments, thereby investigating the relationships between lacustrine organic carbon burial and climate changes. Our findings contribute to the assessment of the role and value of lakes in the global carbon cycle, providing a scientific basis for addressing climate challenges. Concurrently, this research enhances the understanding of the development mechanisms of lacustrine source rock, providing theoretical support for continental oil and gas exploration.

## 2. Geological setting

The Bohai Bay Basin is a rift basin that formed on the Paleozoic North China Craton basement with a latitude range of  $\sim 36\text{--}41^\circ\text{N}$  (Fig. 1A). The basin comprises several subbasins separated by uplifts, including the Jiyang, Bozhong, Liaodong Bay, Liaohe, Huanghua, Jizhong, and Linqing subbasins, each with a distinct history of subsidence and

sedimentation. Among these, the Jiyang Subbasin, situated in the southeastern part of the Bohai Bay Basin, is notable for its high oil production (Fig. 1B; Shi et al., 2019). The Dongying Depression, located in the southern part of the Jiyang Subbasin and is a typical asymmetric half-graben lake basin, with a steep slope in the north and west controlled by faults and a gentle slope in the south and east (Fig. 1C). The Dongying Depression can be subdivided into several secondary structural units, including the Boxing Sag, Lijin Sag, Niuzhuang Sag, Minfeng Sag, the central diapiric anticline, the northern fault zone, and the southern slope belt (Fig. 1C; Li et al., 2025).

The tectonic evolution of the Dongying Depression includes two stages: the Paleogene syn-rift (65.0–24.6 Ma) and the Neogene-Quaternary post-rift stages (24.6 Ma to the present; Feng et al., 2013). The syn-rift strata, which unconformably overlie the Mesozoic strata, comprise the Paleogene Kongdian (Ek), Shahejie (Es), and Dongying (Ed) formations. These strata were primarily deposited in lacustrine environments. The succession of syn-rift strata typically ranges from 4000 m to 7000 m in thickness (Feng et al., 2013). The post-rift strata comprise the Neogene Guantao (Eg) and Minhuazhen (Em) formations, which were deposited primarily in alluvial and fluvial environments (Fig. 1D; Hao et al., 2011; Li et al., 2025).

The Shahejie Formation consists of sandstone, siltstone, mudstone, and evaporite, which are subdivided into four members from top to bottom: The Es1, Es2, Es3, and Es4 members. These strata are stable in the Dongying Depression, and the base of each member of the Shahejie Formation can be traced throughout the depression (Li et al., 2025). Of these, the Es3 Member can be further divided into the Upper Es3 (Es3U), Middle Es3 (Es3M), and Lower Es3 (Es3L) units, and the Es4 Member can be further divided into Upper Es4 (Es4U) and Lower Es4 (Es4L) units (Fig. 1D). The present study focuses on the Es4U unit, the lower part of the Es3L unit, and the upper part of the Es4L unit and mainly consists of interbedded black shale and dark grey calcareous mudstone intercalated with some argillaceous limestone that were deposited in a semi-deep and stratified lake environment (Figs. 1D and 2; Feng et al., 2013; Li et al., 2025). The boundary of Es3L and Es4U units is unconformable at the basin margins but conformable in the basin depocenter (Li et al., 2025). According to the isotopic dating of volcanic rocks, the age of the boundary of Es3L and Es4U units was suggested to be  $\sim 42.4$  Ma (Yao et al., 1994). A recent magnetostratigraphic study correlated the Es3L and Es4U units to Chrons C18n.1n–C20n and suggested that the boundary of the Es3L and Es4U units lies near the base of C19n (Fig. 2; Shi et al., 2019).

## 3. Data and methods

The gamma-ray (GR) logging data from the FY1 and NY1 wells were collected by Sinopec Shengli Oilfield, with a resolution of 0.125 m. GR data can capture the primary signals related to climate change and has a high signal-to-noise ratio, making it widely used in time series analysis (Li et al., 2019). These two wells exhibit unambiguous stratigraphic isochronism, particularly regarding the boundary between the Es4 and Es3 members. Furthermore, despite differences in the thicknesses of correlative intervals, their GR change patterns are analogous, and the general trends of CIA values are consistent (Fig. 2). The NY1 well was continuously cored from 3295 m to 3497 m with a recovery rate of  $\sim 92\%$ . Cores were split vertically and scanned using an Itrax XRF core scanner with a high spatial resolution of 0.0005 m to acquire concentration data for 44 elements.

Core photographs of the Es3 and Es4 shales in the Dongying Depression display a regular alternation of light and dark (Fig. S1). This cyclicity is evident in variations in grayscale variations, GR logs, mineral composition, and elemental abundances (Figs. S1 and S2). It is noteworthy that the thickness of these cycles is  $\sim 1.5$  m, which may correspond to precession cycles, implying that their formation may be influenced by astronomical forcing (Zhang et al., 2022; Li et al., 2025). Cyclostratigraphic analyses were conducted using the high-resolution

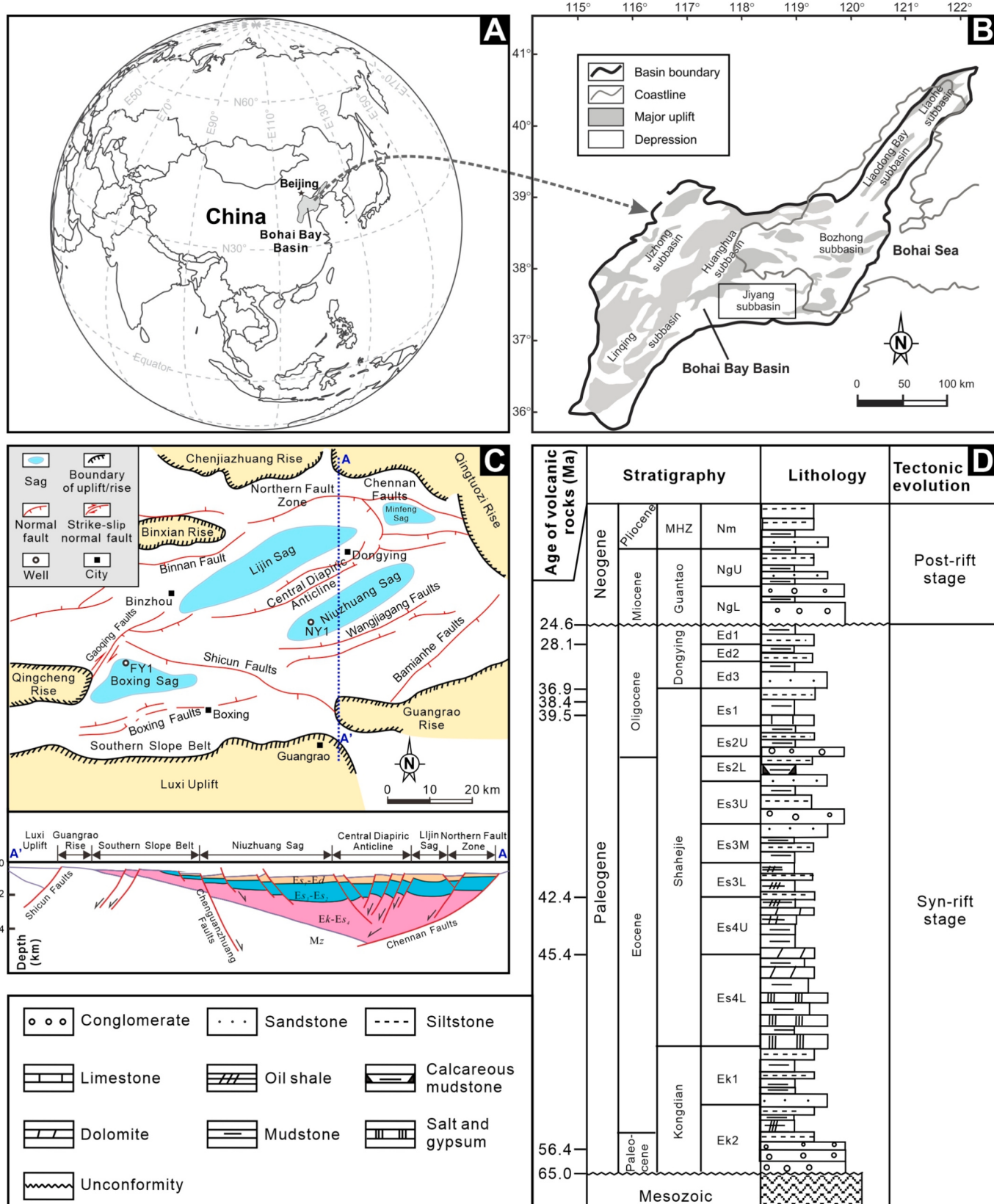


**Fig. 1.** (A) Regional index map showing the location of the Bohai Bay Basin, eastern China. (B) Subbasins of the Bohai Bay Basin (Hao et al., 2011). (C) Structural map of the Dongying Depression showing the location of the NY1 and FY1 wells, and cross-section A-A'. (D) Generalized stratigraphy of the Dongying Depression. Modified from Feng et al., 2013. Volcanic rock ages were obtained from Yao et al. (1994). MHZ = Minghuazhen.

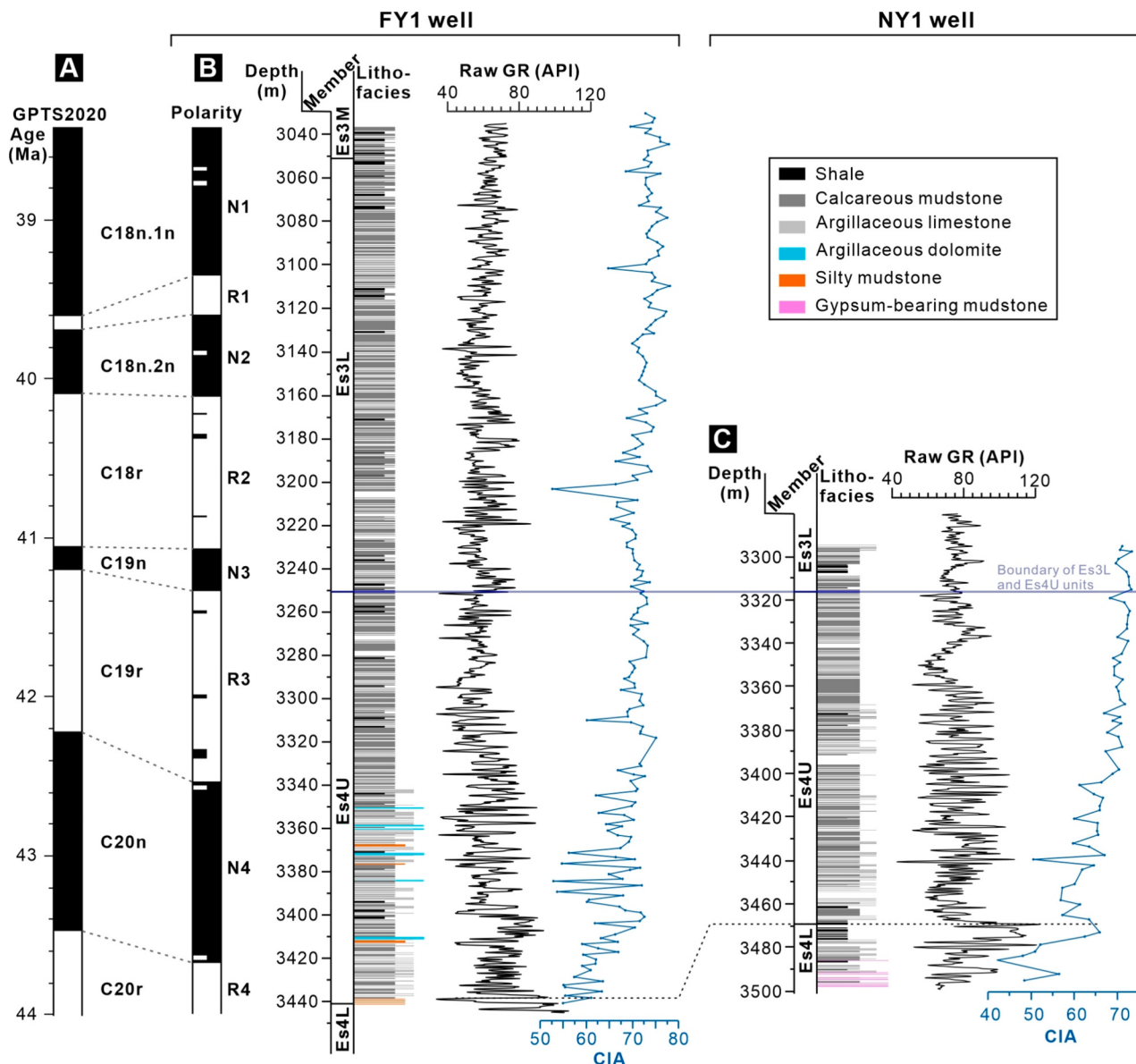


**Fig. 2.** (A) Geomagnetic polarity time scale 2020 (Gradstein et al., 2020). (B) Polarity column, lithofacies, gamma-ray (GR), and chemical index of alteration (CIA) of the FY1 well. Paleomagnetic data are from Shi et al., 2019. (C) Lithofacies, GR, and CIA of the NY1 well.

GR logging data from the FY1 and the NY1 wells, supplemented by XRF-Fe series from the NY1 well. Magnetostratigraphic and cyclostratigraphic analyses of the FY1 well enabled the establishment of an absolute astronomical time scale (ATS), determining the boundary age of the Es3L and Es4U units, which served as an anchor age for the NY1 well. Time series analysis was conducted using Acycle v2.4 software (Li et al., 2019), and the methods are summarized in Supplementary Text 1.

High-resolution sampling was performed on the NY1 well cores. During sampling, sparry calcite veins were avoided. Samples were cut from the fresh core section and crushed to ~200 mesh in an agate mortar and pestle. These samples were analyzed for mineral composition, total organic carbon (TOC), and elemental concentrations. Details are described in Supplementary Text 2. Under the constraint of the absolute ATS, the mineralogical and geochemical proxies were transformed from the depth-domain to the time-domain, with each value being assigned a temporal meaning.

## 4. Results

### 4.1. Time series analyses

A floating astronomical time scale (ATS) was obtained through time series analysis of the GR series from the FY1 well. The magnetic reversal polarity zones (i.e., N4, R3, N3, R2, N2, R1, and N1) in FY1 well were calibrated to magnetic polarity ages of GPTS2020 (Chron C20n to Chron C18n.1n; Gradstein et al., 2020). By fixing the floating ATS at the boundary age of the C18r/C19n from GPTS2020, an absolute ATS (43.62–38.59 Ma) was established. Details have been described in Li et al. (2025) and are summarized in Supplementary Texts 3 and 4, and Figs. S4–S6.

The MTM power spectrum analysis of the untuned GR series of the NY1 well exhibits significant peaks at the 33.3–19.6 m, 9.9–5.2 m, 3.8–2.2 m, and 1.8–1.4 m wavelengths (Fig. S7). Similarly, the MTM power spectrum analysis of the untuned XRF-Fe series also reveals significant peaks at 34.8–19.8 m, 10.2–5.7 m, 3.8–2.2 m, and 1.7–1.4 m wavelengths, all exceeding the 95% confidence level (Fig. S8). The

evolutionary FFT spectrograms of both the untuned GR and XRF-Fe series exhibit  $\sim 34\text{--}29$  m wavelength (Figs. S7 and S8). Correlation coefficient (COCO) analysis of the GR series of the NY1 well reveals a predominant peak at 5.6–5.9 cm/kyr and 8.0–9.5 cm/kyr with null hypothesis significance levels close to 0.001. Similarly, the COCO analysis of the XRF-Fe series reveals a predominant peak at 6.9–7.8 cm/kyr and 9.5 cm/kyr with null hypothesis significance levels close to 0.001. The sedimentation rates generated by the evolutionary correlation coefficient (eCOCO) method are generally consistent with the COCO analysis (Fig. S9). According to the results of COCO and eCOCO analyses, the detected cycles were assigned to specified astronomical parameters. The  $\sim 30$  m, 9.9–5.2 m, 3.8–2.2 m, and 1.8–1.4 m cycles in the MTM power spectrum correlate with long eccentricity (405 kyr), short eccentricity ( $\sim 100$  kyr), obliquity ( $\sim 40$  kyr), and precession ( $\sim 20$  kyr), respectively. A Gaussian bandpass filter was applied to isolate the  $\sim 31.25$  m cycle, which was then tuned by fixing their duration to 405 kyr long-eccentricity cycles, producing a floating ATS with a duration of  $\sim 5.03$  Myr. The MTM power spectra of the tuned GR and XRF-Fe series display significant peaks at periods of 405 kyr,  $\sim 100$  kyr,  $\sim 40$  kyr, and  $\sim 20$  kyr. By fixing the floating ATS at 41.237 Ma (the boundary age of the Es3L and Es4U units), an absolute ATS was established, constraining the succession in the NY1 well to 40.99–43.81 Ma (Fig. S10).

#### 4.2. Mineral composition

The studied shale sequences in the Dongying Depression exhibit a high carbonate mineral content, dominated by calcite, which ranges from 1% to 80% with an average of 35.71%. Dolomite content ranges from 0% to 94%, averaging 11.63%. Siderite content is low, averaging 0.55%. Detrital minerals primarily comprise clay (ranging from 2% to 59%, averaging 22.04%) and quartz (ranging from 0% to 54%, averaging 22.27%). In lacustrine basins, quartz predominantly originates from terrestrial input, and its content serves as a proxy for terrigenous input intensity (Ma et al., 2016). Clay minerals are predominantly illite, with subordinate illite-smectite mixed layers; kaolinite and chlorite contents are relatively low, with kaolinite mainly present in the upper section of the studied sequence. Plagioclase content ranges from 0% to 22%, with an average of 4.32%, and K-feldspar content is relatively low, with an average of 0.08% (Fig. S11). Compared to K-feldspar, plagioclase is more susceptible to alteration into clay minerals during chemical weathering (Nesbitt and Young, 1982), providing supplementary evidence for changes in chemical weathering intensity. Pyrite is ubiquitous in the studied samples, averaging 2.80%. Pyrite can form in the water column or sediment, and its content is closely related to the redox state (Wilkin and Arthur, 2001). Particularly fine frambooidal pyrite typically indicates a syngenetic origin (Fig. S12), and its enrichment level can be used to infer the redox state of the water column (Zou et al., 2018). Since detailed analyses of frambooidal pyrite size and morphology were not performed, this study utilized pyrite content as a supplementary redox proxy. In addition, the shale contains small amounts of gypsum, anhydrite, and barite, with averages of 0.02%, 0.52%, and 0.11%, respectively (Fig. S11). A tripartite compositional classification (carbonate, quartz + feldspar, and clay end-members) was employed to categorize mineralogical facies. A 50% threshold delineates four primary mineralogical facies: felsic shale, clay shale, calcareous shale, and mixed shale. The ternary diagram shows that the studied sequences are predominantly calcareous and mixed shales, with only a minor component of clay and felsic shales (Fig. S11).

#### 4.3. Geochemical proxies

The chemical index of alteration (CIA) was used to evaluate paleoclimate and weathering conditions, with high values indicating more humid and warmer conditions (Nesbitt and Young, 1982). CIA is calculated using molar percentages of major element oxides according to the formula:  $CIA = Al_2O_3 / (Al_2O_3 + Na_2O + K_2O + CaO^*) \times 100$ , where

$CaO^*$  is the concentration of  $CaO$  in silicates (Nesbitt and Young, 1982). The CIA values of the measured samples range from 42.15 to 73.41, displaying an upward-increasing trend through the studied sequence with marked variability in the lower section (Fig. 3A).

The  $Sr/Ba$  ratio is an effective proxy for the salinity of the sedimentary systems (Lan et al., 1987). Similarly, the  $B/Ga$  ratio in argillaceous sediments can be employed to distinguish water salinity, with marine sediments exhibiting markedly elevated  $B/Ga$  values compared to freshwater sediments (Ma et al., 2016; Wei et al., 2021). The variation trends of the  $Sr/Ba$  and  $B/Ga$  ratios are basically the same, characterized by elevated values and pronounced variability in the lower section of the studied sequence, followed by a gradual decrease (Fig. 3C).

Redox-sensitive trace metals exhibit strong enrichment under reducing conditions, with uranium (U) enrichment providing independent constraints on redox conditions (Tribovillard et al., 2006). Paleo-redox evaluations are typically conducted using Al-normalized element ratios to compensate for the effect of dilution by clastic sedimentation (Tribovillard et al., 2006).  $U/Al$  and  $U_{EP}$  values are relatively high in the lower section of the studied sequence, showing an overall decreasing trend upwards though a distinct minimum occurs at  $\sim 43.5$  Ma (Fig. 3D). The sulfur/iron (S/Fe) ratio was employed as an additional redox proxy, displaying a gradual upward-decreasing trend (Fig. 3D). The pristane/phytane (Pr/Ph) ratio serves as a redox indicator, with lower values reflecting more anoxic conditions (Didyk et al., 1978). Pr/Ph ratios of the measured samples range from 0.33 to 1.78, showing an upward-increasing trend through the studied sequence (Fig. 3D).

Iron (Fe), cadmium (Cd), and barium (Ba) were employed to assess primary productivity. However, these elements may originate from both detrital and authigenic sources. Therefore, authigenic Fe and Cd concentrations (denoted as  $Fe_{xs}$  and  $Cd_{xs}$ , respectively) were estimated by subtracting the detrital fraction from total concentration according to the formula:  $X_{xs} = X_{sample} - Al_{sample} \times (X/Al)_{background}$  (Tribovillard et al., 2006). The background values refer to the composition of the upper continental crust in the North China Platform (Yan et al., 1997). Since the Ba element was measured through XRF core scanning, the Al-normalized elemental ratio ( $Ba/Al$ ) was used to eliminate the influence of detrital sources. Results show that all three proxies exhibited relatively low values in the lower section of the studied sequence, followed by a gradual upward increase (Fig. 3E).

The ratios of long-chain and short-chain *n*-alkanes, such as the terrigenous-to-aquatic ratio ( $TAR = (nC_{27} + nC_{29} + nC_{31}) / (nC_{15} + nC_{17} + nC_{19})$ ),  $nC_{25-36}/nC_{13-21}$ ,  $nC_{21-}/nC_{22+}$ ,  $nC_{21-22}/nC_{28-29}$ , and  $nC_{17}/nC_{31}$ , are widely utilized to determine organic matter sources. High TAR and  $nC_{25-36}/nC_{13-21}$  values indicate a higher input of terrigenous organic matter (TOM), whereas high  $nC_{21-}/nC_{22+}$ ,  $nC_{21-22}/nC_{28-29}$ , and  $nC_{17}/nC_{31}$  values reflect a greater contribution of aquatic organic matter (AOM) (Eglinton and Hamilton, 1967; Meyers, 1997; Li et al., 2021). The measured TAR values range from 0.25 to 1.84, with most values in the middle section of the studied sequence exceeding 1.0 (Fig. 3E). The  $nC_{25-36}/nC_{13-21}$  ratio exhibits a similar trend to TAR values, with higher values observed in the middle section of the studied sequence. Conversely, the  $nC_{21-}/nC_{22+}$ ,  $nC_{21-22}/nC_{28-29}$ , and  $nC_{17}/nC_{31}$  ratios display opposite trends, with lower values in the middle section of the studied sequence (Fig. S13). The main peak carbon number of *n*-alkanes can serve as an indicator of organic matter sources, as *n*-alkanes derived from higher plants typically exhibit a predominance of higher carbon numbers (Meyers, 1997). In the studied sequence, the main peak carbon numbers of *n*-alkanes in the lower section range from  $nC_{16}$  to  $nC_{19}$ , while those in the middle section shift towards higher carbon numbers, with a distribution between  $nC_{25}$  and  $nC_{28}$ , indicating a pronounced preference for high-carbon compounds. In contrast, the upper section displays the main peak carbon number of *n*-alkanes ranging from  $nC_{15}$  to  $nC_{17}$  (Fig. 3E).

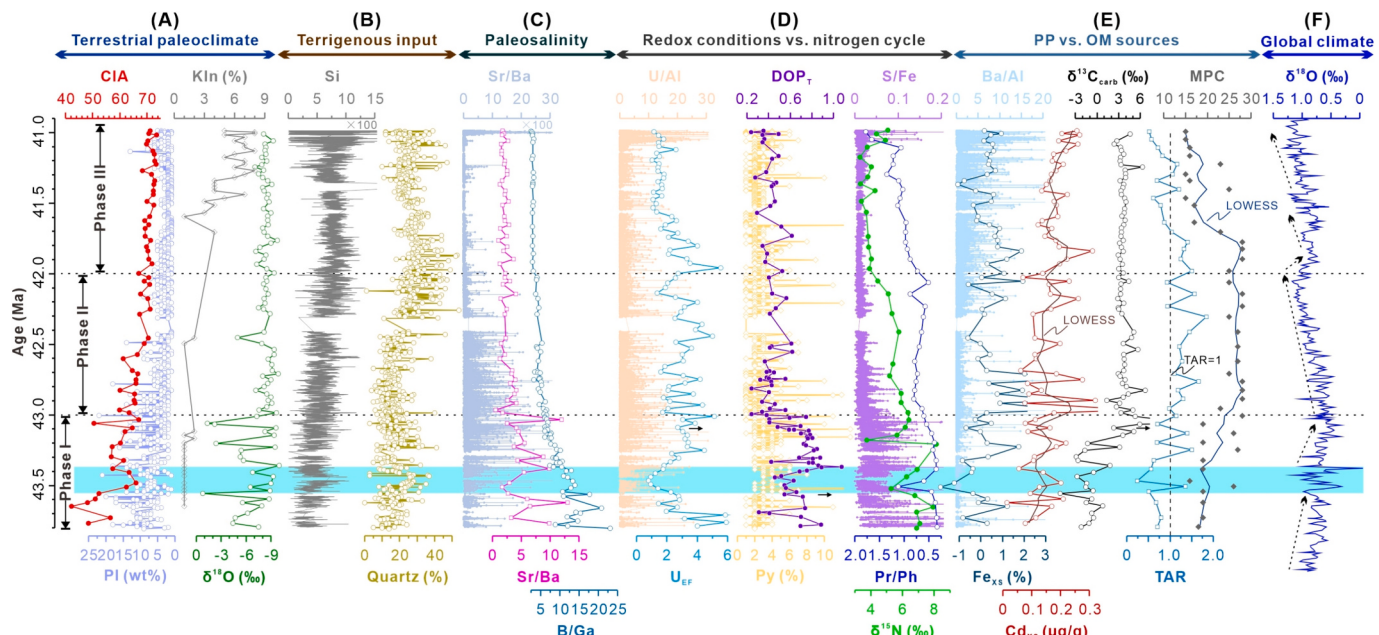


**Fig. 3.** Integrated terrestrial paleoclimatic and paleoenvironmental records in the Dongying Depression of the Bohai Bay Basin, East Asia, and their comparisons with global climate records. (A) Terrestrial paleoclimate records reveal that the paleoclimate in the Bohai Bay Basin during the middle Eocene experienced two transitions at  $\sim 43$  Ma and  $\sim 42$  Ma, thus being divided into three phases. CIA = chemical index of alteration. PI = plagioclase. Kln = kaolinite. Data of calcite oxygen isotopes ( $\delta^{18}\text{O}$ ) are from Ma et al., 2019. (B) Terrigenous input intensity is reflected by Si abundance and quartz content. (C) The Sr/Ba and B/Ga ratios reflect that the paleolake salinity was controlled by paleoclimate changes. (D) Variations in the redox conditions of paleolake bottom water are characterized by redox-sensitive elements, pyrite content,  $\text{DOP}_T$  (the ratio of pyrite Fe to total Fe), S/Fe ratios, and pristane/phytane (Pr/Ph) ratios. Nitrogen biogeochemical cycling of paleolake reflected by nitrogen isotopes ( $\delta^{15}\text{N}$ ), data are from Wei et al., 2021. (E) Changes in primary productivity and organic matter sources of paleolake as reflected by elemental, isotopic, and n-alkanes proxies.  $\text{Fe}_{\text{xs}}$  and  $\text{Cd}_{\text{xs}}$  represent the authigenic fractions of Fe and Cd, respectively. Brown smoothed curves are fitted using the locally weighted scatterplot smoothing (LOWESS) method with Matlab. PP = primary productivity. OM = organic matter. TAR = terrigenous-to-aquatic ratio, defined as  $\text{TAR} = (\text{nC}_{27} + \text{nC}_{29} + \text{nC}_{31}) / (\text{nC}_{15} + \text{nC}_{17} + \text{nC}_{19})$ . MPC = main peak carbon number of n-alkanes. Blue smoothed curves are fitted using the locally weighted scatterplot smoothing (LOWESS) method with Matlab. Carbon isotope data of carbonate ( $\delta^{13}\text{C}_{\text{carb}}$ ) are from Ma et al., 2019. (F) Benthic foraminiferal oxygen isotope ( $\delta^{18}\text{O}$ ) as a proxy for Eocene global paleoclimate. Data are from Westerhold et al., 2020. The blue shaded area represents a possible environmental disturbance. (For interpretation of the references to colour in this figure legend, the reader is referred to the web version of this article.)

## 5. Discussion

### 5.1. Terrestrial paleoclimate

#### 5.1.1. Paleoclimate evolution

During  $\sim 43.8$  Ma to  $\sim 43$  Ma, low CIA values reflect weak chemical weathering under long-term arid climatic conditions. From  $\sim 43$  Ma to  $\sim 42$  Ma, CIA values exhibit a gradual increase, suggesting enhanced chemical weathering and a transition to warmer and more humid climatic conditions (Fig. 3A). After  $\sim 42$  Ma, elevated CIA values indicate strong chemical weathering under warm and humid climatic conditions. Climatic conditions inferred from the variations in kaolinite and plagioclase contents align closely with the CIA record (see Supplementary Text 5 for details). Carbonate  $\delta^{18}\text{O}$  values primarily reflect the combined effects of evaporation and moisture sources (see Supplementary Text 6 for details). Enhanced East Asian monsoons typically signify changes in moisture sources, along with warmer and more humid climatic conditions (weaker evaporation), both of which can result in similar oxygen isotope effects. Lower carbonate  $\delta^{18}\text{O}$  values primarily reflect intensified East Asian monsoon (Ma et al., 2019). Elevated  $\delta^{18}\text{O}$  values during  $\sim 43.8$  Ma to  $\sim 43$  Ma reflect strong evaporation conditions under arid climatic conditions, whereas the gradual decrease in  $\delta^{18}\text{O}$  values from  $\sim 43$  Ma to  $\sim 42$  Ma indicates the increased humidity and weakened evaporation. After  $\sim 42$  Ma,  $\delta^{18}\text{O}$  values remained consistently low, indicating enhanced East Asian Monsoon with warm-humid conditions and decreased reception of high- $\delta^{18}\text{O}$  moisture transported by the westerlies in the study area (Fig. 3A).

#### 5.1.2. Evidence for paleoclimate transitions

The integrated mineralogical and geochemical evidence delineates a three-stage paleoclimate evolution pattern, with transitions occurring at  $\sim 43$  Ma and  $\sim 42$  Ma, respectively (Fig. 3A). Notably, evolutionary FFT spectra of the tuned GR and XRF-Fe series also reveal a significant shift in dominant orbital cycle type (Fig. S10). Specifically, there was a transition from eccentricity- to obliquity-dominated orbital forcing at  $\sim 43$  Ma, followed by a shift back to eccentricity-dominated orbital forcing at  $\sim 42$  Ma (Fig. S10). Obliquity cycles primarily regulate high-latitude insolation, whereas their direct impact on mid- to low-latitude insolation is minimal compared to precession, which is modulated by eccentricity (Bosboom et al., 2014; Bosmans et al., 2015). The Dongying Depression ( $37^{\circ}\text{N}$ - $38^{\circ}\text{N}$ ) is located in mid-latitudes, where obliquity-dominated cyclicity is rarely documented in middle-late Eocene strata. However, obliquity signals can be amplified in mid- to low-latitudes through high-latitude glaciation or atmospheric and oceanic heat-moisture transport (Bosmans et al., 2015). Therefore, the obliquity-dominant signal observed in our records likely reflects teleconnections to high-latitude climatic cyclicity, which exhibits strong and persistent sensitivity to obliquity (Westerhold and Röhl, 2009; Xiao et al., 2010; Bosboom et al., 2014).

Some studies have shown that obliquity signals have been detected in several Eocene sedimentary records outside high latitudes in response to global temperature fluctuations (Westerhold and Röhl, 2009; Bosboom et al., 2014). Concurrently, a certain amount of sea ice existed in high latitudes during the middle-late Eocene global cooling (Bosboom et al., 2014; Darby, 2014). Modeling experiments suggest that obliquity-driven ice volume variability becomes pronounced during incipient ice sheet formation, amplifying the influence of obliquity on climate

(DeConto and Pollard, 2003). The enhanced obliquity signals in the Bohai Bay Basin during ~43–42 Ma approximately coincide with global cooling and the transient appearance of Northern Hemisphere high-latitude glaciation (Xiao et al., 2010; Bosboom et al., 2014). Therefore, the obliquity forcing on East Asian climate may be realized through the feedback of high-latitude ice sheets. This is because high-latitude ice sheets appear highly sensitive to obliquity forcing and may modulate East Asian climate by changing sea level, land-sea thermal contrast, and temperature gradient (Sun et al., 2015; Levy et al., 2019). By integrating subjective visual observation of mineralogical and geochemical paleoclimate proxies with objective evolutionary FFT spectra analysis of tuned GR and XRF-Fe series, the middle Eocene terrestrial paleoclimate evolution of the Bohai Bay Basin can be divided into three phases, each with a duration of ~1 Myr: Phase I (~43.8–43 Ma), Phase II (~43–42 Ma), and Phase III (~42–41 Ma) (Fig. 3A).

## 5.2. Responses of lake environments to paleoclimate changes

### 5.2.1. Terrigenous input

The quartz content and silicon (Si) abundance are commonly employed as proxies for terrigenous input (Ma et al., 2016). Both proxies display analogous trends, with generally low values in Phase I, gradual increases in Phase II, and generally high values in Phase III (Fig. 3B). These observations indicate that the terrigenous input intensity is modulated by climate change. Notably, sporadic high values in Phase I potentially reflect enhanced mechanical weathering under arid conditions (Bohacs et al., 2003) or the input of aeolian quartz grains (Ma et al., 2016). Terrigenous input peaked during the transition of Phase II and Phase III, coinciding with shifts between dry and humid climatic conditions that drive large influxes of sediment into the lake (Bohacs et al., 2003). However, the terrigenous debris influx did not continue to increase in line with the gradual climatic humidification during Phase III, but maintained a relatively stable high value (Fig. 3B). This is because, as the climate gradually becomes more humid, it likely reached a threshold that triggered significant vegetation growth, leading to pervasive plant development. Vegetation acted as baffles and traps, resulting in minimal terrigenous debris input (Bohacs et al., 2003; Ma et al., 2016).

### 5.2.2. Paleosalinity

The Sr/Ba and B/Ga ratios exhibit a comparable trend, decreasing consistently from Phase I to Phase III. This trend is visually contrasting with paleoclimate proxy records, suggesting that paleoclimate was the predominant control on the salinity variations in the Dongying paleolake (Fig. 3C). Elevated Sr/Ba and B/Ga ratios during Phase I indicate that the paleolake was a saline lake, resulting from net evaporation under warm and arid climatic conditions. Subsequently, as the climate became more humid, increased precipitation brought substantial freshwater influx, resulting in a dilution of the ion concentration and a reduction in lake water salinity (Fig. 3C).

### 5.2.3. Redox condition

The redox state of lake bottom waters significantly influences biogeochemical cycling of key nutrient elements and lacustrine ecosystems (Tribouillard et al., 2006). Multi-proxy records reveal staged evolution in the redox state of the lake bottom water, with two shifts occurring at ~43 Ma and ~42 Ma (details are summarized in Supplementary Text 7). These shifts align temporally with paleoclimate transitions, implying climatic control over the redox state of lake bottom waters.

Theoretically, several mechanisms may independently or collectively drive the redox state shift. It is well established that the mixing of lake waters is inhibited under thermal or chemical stratification, preventing deep water oxygen renewal and inducing bottom water anoxia (Bohacs et al., 2003). Consequently, the anoxic and even sulfidic bottom waters observed in Phase I are primarily attributed to permanent

stratification caused by elevated lake salinity, which was ultimately driven by arid climatic conditions (Fig. 3C). Moreover, climate warming can directly enhance lake stratification, as heat inputs tend to warm near-surface waters, resulting in a lower density of surface water compared to that of deeper water, thereby establishing thermal stratification in lakes (Woolway et al., 2021). Subsequently, as the water salinity decreased and global temperature declined (Fig. 3F; Westerhold et al., 2020), this permanent stratification may have become unstable during Phase II, resulting in a significant increase in oxygen levels (Fig. 3D). Nevertheless, seasonal lake overturn may still have been absent during this phase. With monsoon intensified in Phase III, the seasonality was sufficiently strong to establish regular lake overturn and further destabilize the water stratification, accompanied by a further increase in the oxygen level of the lake water column (Fig. 3D).

## 5.3. Co-evolution of environments and organisms

### 5.3.1. Changes in nitrogen biogeochemical cycle

Nitrogen stable isotope composition ( $\delta^{15}\text{N}$ ) serves as a critical proxy for reconstructing the nitrogen biogeochemical cycle in paleolake systems, providing key insights into the co-evolution of lake environments and organisms. In modern freshwater lakes, the  $\delta^{15}\text{N}$  values typically range from 0‰ to 6‰, while alkaline lakes ( $\text{pH} > 9$ ) exhibit significantly elevated values due to enhanced ammonia volatilization (Stüeken et al., 2019; Xia et al., 2022). Generally, a  $\delta^{15}\text{N}$  value of ~10–12‰ serves as a demarcation point between alkaline lakes and non-alkaline lakes (Xia et al., 2022). The  $\delta^{15}\text{N}$  values of the studied sequence remain consistently below 9‰, which is characteristic of non-alkaline lakes (Fig. 3D). In this environment,  $\delta^{15}\text{N}$  values are primarily controlled by denitrification processes, which preferentially release isotopically light  $\text{N}_2$  to the atmosphere, while the remaining  $\text{NO}_3^-$  or  $\text{NO}_2^-$  becomes more enriched in  $^{15}\text{N}$  (Quan et al., 2013). For example, marine sediments may exhibit values of up to 15‰ in the upwelling areas characterized by a high degree of denitrification (Stüeken et al., 2019).

As previously discussed, an increase in water salinity intensifies lake stratification, leading to stagnation and deoxygenation of the lake bottom water. In such conditions, denitrification in the water column is enhanced (Quan et al., 2013). Consequently, the elevated  $\delta^{15}\text{N}$  values observed in Phase I are associated with stronger denitrification in the water column (Fig. 3D). Subsequently, as the climate became more humid, increased precipitation diluted lake water salinity. Particularly during Phase III, intensified monsoon-driven lake overturn increased oxygen levels in the water column, shifting denitrification primarily to the sediments (Kessler et al., 2014; Xia et al., 2022). However, nitrogen isotope fractionation caused by denitrification in sediments is limited, resulting in the  $\delta^{15}\text{N}$  values closer to those of the original fixed nitrogen (Kessler et al., 2014). This explains why the  $\delta^{15}\text{N}$  values in Phase III approximate the average  $\delta^{15}\text{N}$  value of ~3‰ observed in modern freshwater lake sediments (Fig. 3D; McLauchlan et al., 2013). Therefore, the observed  $\delta^{15}\text{N}$  variations in the studied sequence, which correlate with salinity and redox conditions, are most likely attributable to changes in the intensity of denitrification in the water column. In turn, changes in  $\delta^{15}\text{N}$  values provide key evidence for shifts in the salinity and redox conditions.

### 5.3.2. Changes in primary productivity

Several geochemical proxies were employed to assess primary productivity (details are summarized in Supplementary Text 8). These proxies exhibited relatively low values during Phase I, followed by a high-value interval at the onset of Phase II and a gradual decline thereafter. In contrast, Phase III displayed consistently elevated values (Fig. 3E). This implies that primary productivity was generally low in Phase I but experienced a marked increase during Phase II and Phase III. In addition, during periods of high primary productivity, algal photosynthesis preferentially utilizes lighter carbon isotopes ( $^{12}\text{C}$ ), resulting in the enrichment of heavier carbon isotopes ( $^{13}\text{C}$ ) in the dissolved

inorganic carbon pool (DIC) of surface waters, thereby enhancing  $^{13}\text{C}$  enrichment in primary lacustrine carbonates (Hollander et al., 1993; Gonçalves, 2002). Consequently, the positive excursion of carbonate carbon isotopes values ( $\delta^{13}\text{C}_{\text{carb}}$ ) serves as a reliable indicator of increased primary productivity (Gonçalves, 2002). Low  $\delta^{13}\text{C}_{\text{carb}}$  values in Phase I imply relatively low primary productivity, whereas the increased  $\delta^{13}\text{C}_{\text{carb}}$  values in Phase II and Phase III reflect elevated primary productivity (Fig. 3E).

### 5.3.3. Changes in organic matter sources

Phase I is characterized by low TAR values (generally  $<1$ ) and low  $n\text{C}_{25-36}/n\text{C}_{13-21}$  ratios, but high  $n\text{C}_{21-}/n\text{C}_{22+}$ ,  $n\text{C}_{21-22}/n\text{C}_{28-29}$ , and  $n\text{C}_{17}/n\text{C}_{31}$  ratios, coupled with a lower main peak carbon number of *n*-alkanes. This suggests that the organic matter deposited during this period was primarily sourced from algae and bacteria (Figs. 3E and S13). Notably, productivity in Phase I may have been intermittently elevated, coinciding with high  $\delta^{15}\text{N}$  values and strong reducing conditions (Fig. 3D). This indicates active biogeochemical cycling of nutrients due to hypoxic bottom waters, which potentially led to algal blooms. Consequently, internal nutrient recycling may serve to maintain lake primary productivity under limited external nutrient input.

The abrupt increase in primary productivity at the onset of Phase II may be attributable to a rapid transition from arid to humid climatic conditions. Enhanced terrigenous input delivered abundant terrestrial nutrients, stimulating algal blooms. However, despite sustained humid conditions, primary productivity did not increase further, as it was suppressed by concurrent global cooling (Fig. 3E; Westerhold et al., 2020). High TAR values (generally  $>1$ ) and  $n\text{C}_{25-36}/n\text{C}_{13-21}$  ratios, combined with low  $n\text{C}_{21-}/n\text{C}_{22+}$ ,  $n\text{C}_{21-22}/n\text{C}_{28-29}$ , and  $n\text{C}_{17}/n\text{C}_{31}$  ratios, along with higher main peak carbon number of *n*-alkanes, indicate that organic matter deposited during this period was predominantly TOM (Figs. 3E and S13). Additionally, high TOM influx may

significantly accelerate mineralization of autochthonous organic matter in lakes (Yang et al., 2022). Collectively, these processes contributed to the predominance of TOM during Phase II.

Under humid climatic conditions, increased runoff results in elevated terrigenous inputs, transporting substantial nutrients to the lakes during Phase III. Seasonal lake overturn may further improve nutrient cycling efficiency (Gonçalves, 2002). These factors collectively sustain long-term high primary productivity. Despite high TOM input during Phase III, low TAR values and low  $n\text{C}_{25-36}/n\text{C}_{13-21}$  ratios, along with high  $n\text{C}_{21-}/n\text{C}_{22+}$ ,  $n\text{C}_{21-22}/n\text{C}_{28-29}$ , and  $n\text{C}_{17}/n\text{C}_{31}$  ratios, combined with lower main peak carbon number of *n*-alkanes, imply that TOM constituted a minor proportion, indirectly indicating high AOM production (Figs. 3E and S13). The role of enhanced monsoons in elevating productivity is well documented; for example, the Indian monsoon is known to boost biological productivity in the Arabian Sea (Le Mézo et al., 2017).

### 5.4. Organic carbon burial linked to global and regional climate changes

The reconstructed temporal variations of the organic carbon burial rate (OCBR) in the Dongying paleolake exhibit significant fluctuations during the middle Eocene. Phase I displays an overall increasing trend, peaking at the transition to Phase II, followed by a gradual decline until the onset of Phase III. During Phase III, the OCBR increases again and stabilizes at a relatively high value (Fig. 4A). Although OC burial in lakes is governed by complex physical, chemical, and biological interactions, primary productivity and bottom water redox conditions are the predominant controls (Sobek et al., 2009; Mendonça et al., 2017). As discussed previously, shifts in these controls reflect responses to terrestrial climate change. Therefore, the middle Eocene OCBR variations in the Dongying paleolake ultimately reflect a response to terrestrial climate change, modulated by global climate and regional factors.

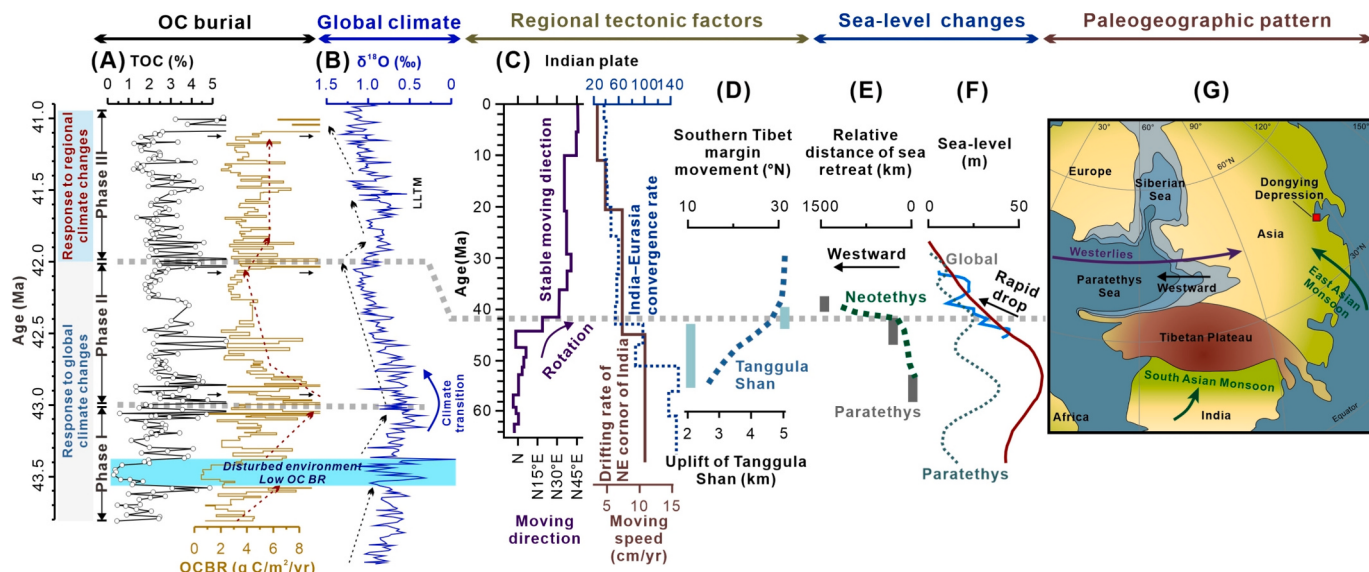


**Fig. 4.** Diagram showing the response of organic carbon burial in the Dongying paleolake (East Asia) during the Eocene to global and regional forcing factors, and the concurrence or coupling of these factors. Global climate changes in combination with the Tibetan Plateau uplift and Paratethys Sea retreat jointly shaped the three phases of East Asian terrestrial paleoclimate. (A) Changes in total organic carbon content. Temporal variations of the organic carbon burial rate. OC = organic carbon. OCBR = organic carbon burial rate. (B) Benthic foraminiferal oxygen isotope ( $\delta^{18}\text{O}$ ) as a proxy for Eocene global paleoclimate. Data are from Westerhold et al., 2020. (C) Purple and brown solid lines represent the moving direction and speed of the Indian plate during the Cenozoic, respectively (after Molnar and Stock, 2009; Fang et al., 2021). The blue dashed line shows reconstructions of the India-Eurasia convergence rate, modified from van Hinsbergen et al., 2011. (D) The northward movement of the southern margin of the Tibetan Plateau, calibrated for the reference point (29°N, 88°E) in the Gangdese Shan (after Tan et al., 2010; Chen et al., 2014; Dawen and Maodu, 2019; Fang et al., 2021). (E), (F) Westward retreat and sea-level drop of the Neotethys and Paratethys seas (after Meijer et al., 2019; Fang et al., 2021), and their comparison with global sea-level changes (after Miller et al., 2005; Cramer et al., 2011). (G) Paleogeographic and paleoclimatic pattern of Asia during the Eocene, modified from Meijer et al., 2019. LLTM = the Late Lutetian Thermal Maximum. (For interpretation of the references to colour in this figure legend, the reader is referred to the web version of this article.)

#### 5.4.1. Phase I and phase II: Response to global climate changes

The OCBR variations during Phase I and Phase II exhibit broad consistency with contemporary global climate trends (Figs. 4A and B). The increase in OCBR during Phase I is coupled with global warming. Considering East Asia paleoclimatic patterns, global warming during Phase I likely triggered a northward shift of the subtropical highs (Lu and Reichler, 2007; Guo et al., 2008). In this scenario, net evaporation leads to lake water concentration and elevated salinity, which strengthens lake stratification. Lake stratification regulates organic matter production and degradation by affecting internal nutrient cycling efficiency and dissolved oxygen concentration in water column (Fig. 5). Although warming can enhance OC mineralization and reduce OC burial efficiency, it may simultaneously increase aquatic and terrestrial biomass, potentially enhancing OC burial. We propose that the salinity stratification during Phase I enhanced organic matter preservation, thereby allowing the OC deposition rate to exceed the decomposition rate and leading to a net increase in OC burial. This mechanism represents the primary control on OC burial during this stage. Notably, the transient OCBR decline at ~43.5 Ma coincides with environmental perturbations caused by significant fluctuations in global climate, evidenced by strong fluctuations in CIA values, salinity proxies, U<sub>EF</sub>, Pr/Ph, and δ<sup>15</sup>N values (blue shaded area in Figs. 3 and 4). Concurrently, a significant negative δ<sup>13</sup>C<sub>org</sub> excursion was documented in the continental basins of inland China (Zhao et al., 2022), while several regions globally also show disrupted shallow-marine and lacustrine diatomite accumulation (Figus et al., 2024). These contemporaneous anomalies may imply a global climatic perturbation.

During Phase II, global temperatures gradually declined, accompanied by a southward migration of the subtropical highs that triggered a transition from arid to humid climatic conditions (Lu and Reichler, 2007; Guo et al., 2008). This transition caused an increase in terrigenous input, delivering substantial terrestrial nutrients to the lake and enhancing primary productivity at the onset of Phase II (Fig. 5). However, amid persistent global cooling, primary productivity failed to sustain its increase (Fig. 3). Concurrently, orbital forcing transitioned from eccentricity- to obliquity-dominated, resulting in significant orbital-scale climate variability (Fig. S10). Under increasingly humid climatic conditions, lakes received a substantial input of TOM, leading to significant burial of terrigenous OC during Phase II (Figs. 3E and S13). In conclusion, OCBR variations in Phase I and II align closely with global climate, with inflection points in OCBR corresponding to global climate transitions (Fig. 4). Therefore, OC burial in the Dongying paleolake during this period was a response to global climate change (Fig. 5).

#### 5.4.2. Phase III: Response to regional climate changes

The transition from Phase II to Phase III (~42 Ma) was marked by notable shifts in terrestrial paleoclimate and paleolake environments, coinciding with East Asian monsoon intensification. This suggests regional factors exerted a significant influence on lacustrine OC burial during Phase III. The full India-Asia collision and associated Asian paleogeographic reorganization have been proposed as drivers of East Asian monsoon intensification (Fang et al., 2021). Following the initial India-Asia collision at ~55 Ma, the northward movement of the Indian plate underwent a significant decrease and rotation at ~42 Ma, possibly due to the full merging of the Indian and Asian continents in response to strong resistance from the Asian continent (Fig. 4C; Molnar and Stock, 2009; Zheng and Wu, 2018). This triggered pulsed uplift of the Tangula Shan in the central Tibetan Plateau (TP) (Fig. 4D; Wang et al., 2008a; Wang et al., 2008b), which served as a key forcing factor for East Asian monsoon intensification at ~42 Ma, as plateau uplift would create orographic barriers and intensify monsoonal circulation by increasing thermal contrasts and insulating southern moisture (Molnar et al., 2010; Meijer et al., 2019). Concurrently, the transition from obliquity- to eccentricity-dominated orbital forcing at ~42 Ma may also be associated with the uplift of the Tibetan Plateau, as it weakens the teleconnection between low- and mid-latitudes in Asia, making the climate system more

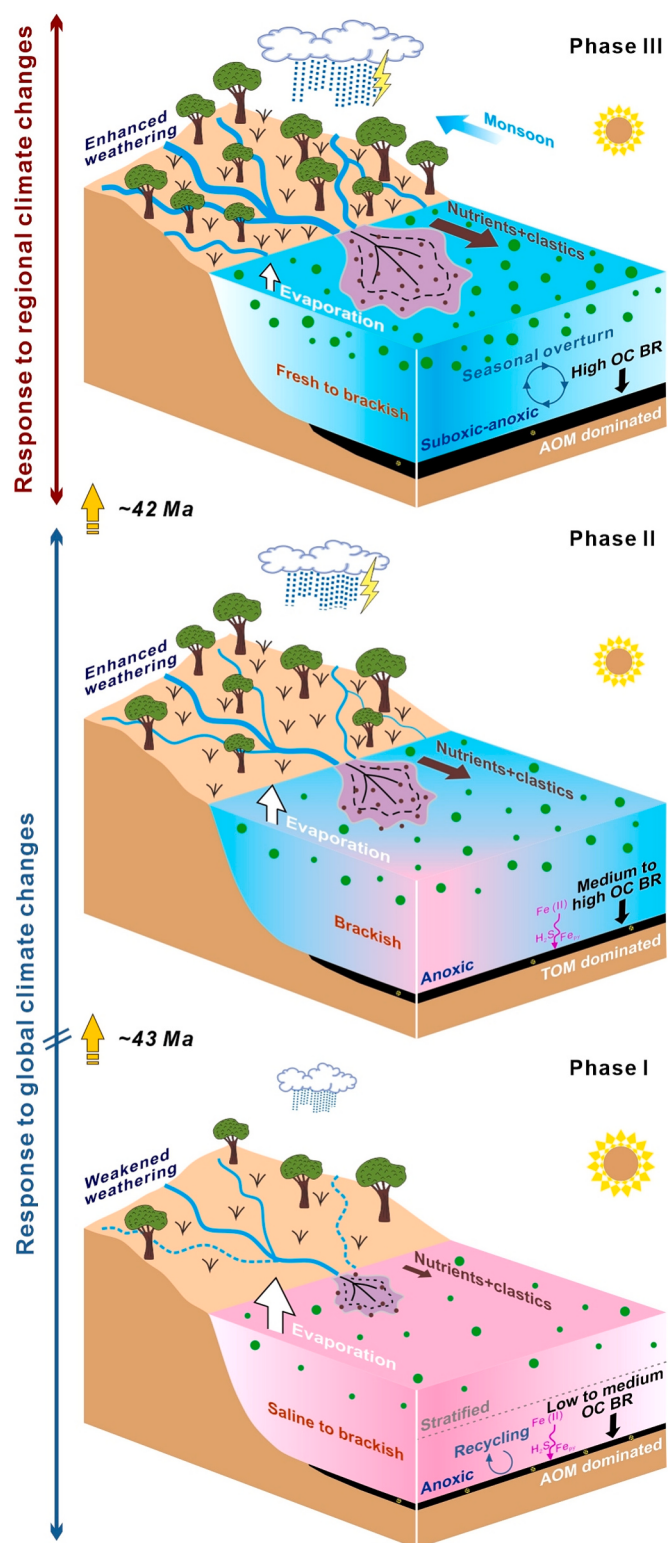


**Fig. 5.** Schematic illustration of paleoenvironmental changes and organic carbon burial in East Asian large paleolakes linked to global and regional climate during the middle Eocene. Climate change regulates primary productivity, lake water salinity, water column stratification, bottom water redox conditions, and biogeochemical cycles by influencing source area weathering, terrigenous input, nutrient supply, and precipitation/evaporation (P/E) ratios, thereby altering the organic carbon burial in lacustrine systems.

sensitive to eccentricity cycles (Fig. S10; Zhang et al., 2024). Additionally, the extent of the Paratethys Sea fluctuated with three progressively diminishing sea incursions that are superimposed on the long-term Eocene global sea-level decline (Figs. 4E and F). Rapid westward retreat of the Paratethys Sea at ~42 Ma, coupled with the synchronous closure of the Neotethys Sea, may have enhanced the land-sea thermal contrasts, intensifying monsoonal circulation over East Asia (Jiao et al., 2023). In conclusion, the concurrence or coupling of multiple factors may have collectively contributed to the significant intensification of the East Asian monsoon (Figs. 4C–G).

In lacustrine systems, elevated OC burial typically requires high aquatic primary productivity. Although anoxic bottom water conditions are crucial for OC preservation, such conditions are often triggered by seasonal algal blooms. Intensified East Asian monsoon will accelerate the hydrological cycle and enhance weathering in source areas, thereby increasing terrestrial nutrient supply, elevating lake primary productivity, and driving substantial OC sequestration (Fig. 5). A recent study reported increased lake primary productivity and OC burial during the early Holocene, driven by monsoon intensification (Zhou et al., 2025). Therefore, the accelerated OCBR in the Dongying paleolake during Phase III is attributed to regional geological events, including paleogeographic and paleoclimatic pattern reorganization. During this period, regional factors superseded global factors as the dominant influences on OC burial. In summary, terrestrial paleoclimate, paleolake environments, and the co-evolution of lake environments and organisms reveal the complex links between the Tibetan Plateau orogeny, climate, environment, biology, and OC burial.

## 6. Conclusions

Multiple lines of evidence indicate that the Eocene paleoclimate evolution in the Bohai Bay Basin exhibits distinct phases, demarcated by climate transitions at ~43 Ma and ~42 Ma. During Phase I (~43.8–43 Ma), the Bohai Bay Basin experienced an arid climate governed by the subtropical high pressure, characterized by low source-area chemical weathering rates and limited terrestrial nutrient input. The lake exhibited elevated salinity, stable water column stratification, and anoxic bottom waters, which enhanced organic matter preservation and served as the dominant control on OC burial during this period. The transition from Phase I to Phase II coincided with a southward shift of subtropical high pressure triggered by global cooling, resulting in a more humid climate and enhanced chemical weathering. During Phase II (~43–42 Ma), the OCBR increased, dominated by terrestrial OC. The onset of Phase III (~42–41 Ma) was primarily associated with regional tectonic-climatic factors, including the Tibetan Plateau uplift and Paratethys Sea retreat, which collectively enhanced monsoon intensity. Intensified monsoon accelerated the hydrological cycle, while strengthened chemical weathering in the source area and increased input of terrestrial nutrients collectively led to a significant rise in primary productivity and OCBR. During this phase, regional climate superseded global climate as the dominant OC burial driver. We propose that the OC burial in the large paleolakes of the Bohai Bay Basin was a response to global and regional climate changes. Substantial OC burial contributed to the formation of lacustrine hydrocarbon source rocks while potentially regulating global climate.

## CRediT authorship contribution statement

**Qiqi Li:** Software, Methodology, Data curation, Conceptualization, Writing – review & editing, Writing – original draft. **Shang Xu:** Validation, Resources, Data curation, Writing – review & editing. **Fang Hao:** Conceptualization, Writing – review & editing.

## Declaration of competing interest

We declare that we have no financial and personal relationships with

other people or organizations that can inappropriately influence our work, there is no professional or other personal interest of any nature or kind in any product, service and/or company that could be construed as influencing the position presented in the manuscript entitled “*Organic carbon burial in a middle Eocene East Asian paleolake: Response to global and regional climate changes*”.

## Acknowledgements

This work was supported by the National Natural Science Foundation of China (42402143 and 42488101), the Basic Research Program of Jiangsu (BK20241667), and the Postdoctoral Fellowship Program of CPSF (GZC20233004). We are grateful to the Sinopec Shengli Oilfield for supporting this research.

## Appendix A. Supplementary data

Supplementary data to this article can be found online at <https://doi.org/10.1016/j.palaeo.2025.113183>.

## Data availability

The data that support the findings of this study are available from the corresponding author upon reasonable request.

## References

- Bohacs, K.M., Carroll, A.R., Neal, J.E., 2003. Lessons from large lake systems-Thresholds, nonlinearity, and strange attractors. *Spec. Pap. Geol. Soc. Am.* 370, 75–90.
- Bosboom, R.E., Abels, H.A., Hoorn, C., et al., 2014. Aridification in continental Asia after the middle Eocene climatic optimum (MECO). *Earth Planet. Sci. Lett.* 389, 34–42.
- Bosmans, J., Hilgen, F., Tuenter, E., et al., 2015. Obliquity forcing of low-latitude climate. *Clim. Past* 11 (10), 1335–1346.
- Cartapanis, O., Bianchi, D., Jaccard, S.L., et al., 2016. Global pulses of organic carbon burial in deep-sea sediments during glacial maxima. *Nat. Commun.* 7 (1), 10796.
- Chen, J., Huang, B., Yi, Z., et al., 2014. Paleomagnetic and  $^{40}\text{Ar}/^{39}\text{Ar}$  geochronological results from the Linzizong Group, Linzhou Basin, Lhasa Terrane, Tibet: Implications to Paleogene paleolatitude and onset of the India–Asia collision. *J. Asian Earth Sci.* 96, 162–177.
- Cramer, B., Miller, K., Barrett, P., et al., 2011. Late Cretaceous–Neogene trends in deep ocean temperature and continental ice volume: Reconciling records of benthic foraminiferal geochemistry ( $^{81}\text{O}$  and Mg/Ca) with sea level history. *J. Geophys. Res. Oceans* 116 (C12).
- Darby, D.A., 2014. Ephemeral formation of perennial sea ice in the Arctic Ocean during the middle Eocene. *Nat. Geosci.* 7 (3), 210–213.
- Dawen, Z., Maodu, Y., 2019. Paleomagnetic constraints on the onset of India-Eurasia collision: a synthesis. *Geol. Rev.* 65 (05), 1251–1268.
- DeConto, R.M., Pollard, D., 2003. Rapid Cenozoic glaciation of Antarctica induced by declining atmospheric CO<sub>2</sub>. *Nature* 421 (6920), 245–249.
- Didyk, B., Simoneit, B., Brassell, S.T., et al., 1978. Organic geochemical indicators of palaeoenvironmental conditions of sedimentation. *Nature* 272 (5650), 216–222.
- Ding, L., Xu, Q., Yue, Y., et al., 2014. The andean-type gangdese mountains: paleoelevation record from the paleocene-eocene Linzhou basin. *Earth Planet. Sci. Lett.* 392, 250–264.
- Eglinton, G., Hamilton, R.J., 1967. Leaf epicuticular waxes. *Science* 156 (3780), 1322–1335.
- Fang, X., Yan, M., Zhang, W., et al., 2021. Paleogeography control of Indian monsoon intensification and expansion at 41 Ma. *Sci. Bull.* 66 (22), 2320–2328.
- Feng, Y., Li, S., Lu, Y., 2013. Sequence stratigraphy and architectural variability in late Eocene lacustrine strata of the Dongying Depression, Bohai Bay Basin, eastern China. *Sediment. Geol.* 295, 1–26.
- Figus, C., Bialik, O.M., Gladenkov, A.Y., et al., 2024. Climatic and tectonic controls on shallow-marine and freshwater diatomite deposition throughout the Palaeogene. *Clim. Past* 20 (11), 2629–2644.
- Gonçalves, F.T., 2002. Organic and isotope geochemistry of the early cretaceous rift sequence in the Camamu Basin, Brazil: paleolimnological inferences and source rock models. *Org. Geochem.* 33 (1), 67–80.
- Gradstein, F.M., Ogg, J.G., Schmitz, M.D., et al., 2020. *Geologic time scale 2020*. Elsevier.
- Guo, Z., Sun, B., Zhang, Z., et al., 2008. A major reorganization of Asian climate by the early Miocene. *Clim. Past* 4 (3), 153–174.
- Hao, F., Zhou, X., Zhu, Y., et al., 2011. Lacustrine source rock deposition in response to co-evolution of environments and organisms controlled by tectonic subsidence and climate, Bohai Bay Basin, China. *Org. Geochem.* 42 (4), 323–339.
- Hollander, D.J., McKenzie, J.A., Hsu, K.J., et al., 1993. Application of an eutrophic lake model to the origin of ancient organic-carbon-rich sediments. *Glob. Biogeochem. Cycles* 7 (1), 157–179.

- Jiao, W., Wan, S., Li, Y.X., et al., 2023. Global cooling-driven summer monsoon weakening in south China across the eocene-oligocene transition. *J. Geophys. Res. Solid Earth* 128 (11) e2023JB027265.
- Kemp, D.B., Suan, G., Fantasia, A., et al., 2022. Global organic carbon burial during the Toarcian oceanic anoxic event: patterns and controls. *Earth Sci. Rev.* 231, 104086.
- Kessler, A.J., Bristow, L.A., Cardenas, M.B., et al., 2014. The isotope effect of denitrification in permeable sediments. *Geochim. Cosmochim. Acta* 133, 156–167.
- Lan, X., Ma, D., Xu, M., et al., 1987. Some geochemical indicators of the Pearl River Delta and their facies significance. *Mar. Geol. Quat. Geol.* 7 (1), 39–49.
- Le Mézo, P., Beaufort, L., Bopp, L., et al., 2017. From monsoon to marine productivity in the Arabian Sea: insights from glacial and interglacial climates. *Clim. Past* 13 (7), 759–778.
- Levy, R., Meyers, S.R., Naish, T.R., et al., 2019. Antarctic ice-sheet sensitivity to obliquity forcing enhanced through ocean connections. *Nat. Geosci.* 12 (2), 132–137.
- Li, M., Huang, C., Ogg, J., et al., 2019. Paleoclimate proxies for cyclostratigraphy: Comparative analysis using a lower Triassic marine section in South China. *Earth Sci. Rev.* 189, 125–146.
- Li, Q., Xu, S., Hao, F., et al., 2021. Geochemical characteristics and organic matter accumulation of argillaceous dolomite in a saline lacustrine basin: a case study from the Paleogene Xingouzui Formation, Jianghan Basin, China. *Mar. Pet. Geol.* 128, 105041.
- Li, Q., Xu, S., Hao, F., 2025. Reassessing the possibility of marine incursion into a paleo-lake under the constraints of a chronological framework: Implications for lake salinization mechanisms. *GSA Bull.* 137 (5–6), 2489–2505.
- Licht, A., Van Cappelle, M., Abels, H.A., et al., 2014. Asian monsoons in a late Eocene greenhouse world. *Nature* 513 (7519), 501–506.
- Lin, J., Dai, J.G., Zhuang, G., et al., 2020. Late Eocene–Oligocene high relief paleotopography in the north central Tibetan Plateau: Insights from detrital zircon U–Pb geochronology and leaf wax hydrogen isotope studies. *Tectonics* 39 (2) e2019TC005815.
- Li, M., Hinnov, L., Kump, L., 2019. Acycle: Time-series analysis software for paleoclimate research and education. *Comput. Geosci.* 127, 12–22.
- Lu, J., Vecchi, G. A. and Reichler, T., 2007. Expansion of the Hadley cell under global warming. *Geophys. Res. Lett.*, 34(6): L06805.
- Ma, Y., Fan, M., Lu, Y., et al., 2016. Climate-driven paleolimnological change controls lacustrine mudstone depositional process and organic matter accumulation: Constraints from lithofacies and geochemical studies in the Zanhua Depression, eastern China. *Int. J. Coal Geol.* 167, 103–118.
- Ma, Y., Fan, M., Lu, Y., et al., 2019. Stable isotope record of middle Eocene summer monsoon and its instability in eastern China. *Glob. Planet. Chang.* 175, 103–112.
- McLauchlan, K.K., Williams, J.J., Craine, J.M., et al., 2013. Changes in global nitrogen cycling during the Holocene epoch. *Nature* 495 (7441), 352–355.
- Meijer, N., Dupont-Nivet, G., Abels, H.A., et al., 2019. Central Asian moisture modulated by proto-Paratethys Sea incursions since the early Eocene. *Earth Planet. Sci. Lett.* 510, 73–84.
- Mendonça, R., Müller, R.A., Clow, D., et al., 2017. Organic carbon burial in global lakes and reservoirs. *Nat. Commun.* 8 (1), 1694.
- Meyers, P.A., 1997. Organic geochemical proxies of paleoceanographic, paleolimnologic, and paleoclimatic processes. *Org. Geochim.* 27 (5–6), 213–250.
- Miller, K.G., Komink, M.A., Browning, J.V., et al., 2005. The Phanerozoic record of global sea-level change. *Science* 310 (5752), 1293–1298.
- Molnar, P., Stock, J.M., 2009. Slowing of India's convergence with Eurasia since 20 Ma and its implications for Tibetan mantle dynamics. *Tectonics* 28 (3), 1–11.
- Molnar, P., Boos, W.R., Battisti, D.S., 2010. Orographic controls on climate and paleoclimate of Asia: thermal and mechanical roles for the Tibetan Plateau. *Annu. Rev. Earth Planet. Sci.* 38 (1), 77–102.
- Nesbitt, H., Young, G., 1982. Early Proterozoic climates and plate motions inferred from major element chemistry of lutites. *Nature* 299 (5885), 715–717.
- Quan, T.M., Adigwe, E.N., Riedinger, N., et al., 2013. Evaluating nitrogen isotopes as proxies for depositional environmental conditions in shales: comparing Caney and Woodford Shales in the Arkoma Basin, Oklahoma. *Chem. Geol.* 360–361, 231–240.
- Shi, J., Jin, Z., Liu, Q., et al., 2019. Cyclostratigraphy and astronomical tuning of the middle Eocene terrestrial successions in the Bohai Bay Basin, Eastern China. *Glob. Planet. Chang.* 174, 115–126.
- Sobek, S., Durisch-Kaiser, E., Zurbrügg, R., et al., 2009. Organic carbon burial efficiency in lake sediments controlled by oxygen exposure time and sediment source. *Limnol. Oceanogr.* 54 (6), 2243–2254.
- Stüeken, E.E., Martinez, A., Love, G., et al., 2019. Effects of pH on redox proxies in a Jurassic rift lake: Implications for interpreting environmental records in deep time. *Geochim. Cosmochim. Acta* 252, 240–267.
- Sun, Y., Kutzbach, J., An, Z., et al., 2015. Astronomical and glacial forcing of East Asian summer monsoon variability. *Quat. Sci. Rev.* 115, 132–142.
- Tan, X., Gilder, S., Kodama, K.P., et al., 2010. New paleomagnetic results from the Lhasa block: Revised estimation of latitudinal shortening across Tibet and implications for dating the India-Asia collision. *Earth Planet. Sci. Lett.* 293 (3–4), 396–404.
- Tranvik, L.J., Downing, J.A., Cotner, J.B., et al., 2009. Lakes and reservoirs as regulators of carbon cycling and climate. *Limnol. Oceanogr.* 54 (6part2), 2298–2314.
- Tribouillard, N., Algeo, T.J., Lyons, T., et al., 2006. Trace metals as paleoredox and paleoproductivity proxies: an update. *Chem. Geol.* 232 (1–2), 12–32.
- van Hinsbergen, D.J., Steinberger, B., Doubrovine, P.V., et al., 2011. Acceleration and deceleration of India-Asia convergence since the cretaceous: Roles of mantle plumes and continental collision. *J. Geophys. Res. Solid Earth* 116 (B6).
- Wang, C., Zhao, X., Liu, Z., et al., 2008a. Constraints on the early uplift history of the Tibetan Plateau. *Proc. Natl. Acad. Sci.* 105 (13), 4987–4992.
- Wang, Q., Wyman, D.A., Xu, J., et al., 2008b. Eocene melting of subducting continental crust and early uplifting of Central Tibet: evidence from central-western Qiangtang high-K calc-alkaline andesites, dacites and rhyolites. *Earth Planet. Sci. Lett.* 272 (1–2), 158–171.
- Wei, W., Lu, Y., Ma, Y., et al., 2021. Nitrogen isotopes as paleoenvironmental proxies in marginal-marine shales, Bohai Bay Basin, NE China. *Sediment. Geol.* 421, 105963.
- Westerhold, T., Röhl, U., 2009. High resolution cyclostratigraphy of the early Eocene—new insights into the origin of the Cenozoic cooling trend. *Clim. Past* 5 (3), 309–327.
- Westerhold, T., Marwan, N., Drury, A.J., et al., 2020. An astronomically dated record of Earth's climate and its predictability over the last 66 million years. *Science* 369 (6509), 1383–1387.
- Wilkin, R.T., Arthur, M.A., 2001. Variations in pyrite texture, sulfur isotope composition, and iron systematics in the Black Sea: evidence for late Pleistocene to Holocene excursions of the  $O_2-H_2S$  redox transition. *Geochim. Cosmochim. Acta* 65 (9), 1399–1416.
- Woolway, R.I., Sharma, S., Weyhenmeyer, G.A., et al., 2021. Phenological shifts in lake stratification under climate change. *Nat. Commun.* 12 (1), 2318.
- Xia, L., Cao, J., Stüeken, E.E., et al., 2022. Linkages between nitrogen cycling, nitrogen isotopes, and environmental properties in paleo-lake basins. *GSA Bull.* 134 (9–10), 2359–2372.
- Xiao, G., Abels, H.A., Yao, Z., et al., 2010. Asian aridification linked to the first step of the Eocene-Oligocene climate transition (EOT) in obliquity-dominated terrestrial records (Xining Basin, China). *Clim. Past* 6 (4), 501–513.
- Xu, W., Ruhl, M., Jenkyns, H.C., et al., 2017. Carbon sequestration in an expanded lake system during the Toarcian oceanic anoxic event. *Nat. Geosci.* 10 (2), 129–134.
- Yan, M., Chi, Q., Gu, T., et al., 1997. Chemical composition of upper crust in eastern China. *Sci. China Ser. D Earth Sci.* 40 (5), 530–539.
- Yang, J., Han, M., Zhao, Z., et al., 2022. Positive priming effects induced by allochthonous and autochthonous organic matter input in the lake sediments with different salinity. *Geophys. Res. Lett.* 49 (5) e2021GL096133.
- Yao, Y., Liang, H., Cai, Z., et al., 1994. Tertiary in Petrolierous Regions of China (IV): The Bohai Gulf Basin. Petroleum Industry Press, Beijing.
- Zhang, J., Jiang, Z., Liang, C., et al., 2022. Astronomical forcing of meter-scale organic-rich mudstone-limestone cyclicity in the Eocene Dongying sag, China: Implications for shale reservoir exploration. *AAPG Bull.* 106 (8), 1557–1579.
- Zhang, Q., Shen, L., Fu, X., et al., 2024. Eocene climate and hydrology of eastern Asia controlled by orbital forcing and Tibetan Plateau uplift. *Earth Planet. Sci. Lett.* 646, 118981.
- Zhao, Y., Wu, F., Fang, X., et al., 2022. Global climate change drove terrestrial ecosystem evolution during the late Paleocene-middle Miocene in the Lanzhou Basin, northeast Tibetan Plateau. *Palaeogeogr. Palaeoclimatol. Palaeoecol.* 598, 111045.
- Zheng, Y., Wu, F., 2018. The timing of continental collision between India and Asia. *Sci. Bull.* 63 (24), 1649–1654.
- Zhou, S., Long, H., Chen, W., et al., 2025. Temperature seasonality regulates organic carbon burial in lake. *Nat. Commun.* 16 (1), 1049.
- Zou, C., Qiu, Z., Wei, H., et al., 2018. Euxinia caused the late Ordovician extinction: evidence from pyrite morphology and pyritic sulfur isotopic composition in the Yangtze area, South China. *Palaeogeogr. Palaeoclimatol. Palaeoecol.* 511, 1–11.